EDGE ARTICLE

Check for updates

Universal linker-free assembly of core–satellite hetero-superstructures†

Yanfang Hu,[a] Yonglong Li,[a] Linfeng Yu,[a] Yuying Zhang, [b] Yuming Lai,[c] Wei Zhang[a] and Wei Xie [*a]

Colloidal superstructures comprising hetero-building blocks often show unanticipated physical and chemical properties. Here, we present a universal assembly methodology to prepare hetero-superstructures. This straightforward methodology allows the assembly of building block materials varying from inorganic nanoparticles to living cells to form superstructures. No molecular linker is required to bind the building blocks together and thus the products do not contain any unwanted adscititious material. The Fourier transform infrared spectra, high resolution transmission electron microscopic images and nanoparticle adhesion force measurement results reveal that the key to self-organization is stripping surface ligands by adding non-polar solvents or neutralizing surface charge by adding salts, which allow us to tune the balance between van der Waals attraction and electrostatic repulsion in the colloid so as to trigger the assembling process. As a proof-of-concept, the superior photocatalytic activity and single-particle surface-enhanced Raman scattering of the corresponding superstructures are demonstrated. Our methodology greatly extends the scope of building blocks for superstructure assembly and enables scalable construction of colloidal multifunctional materials.

Introduction

Assembly of diverse nanoparticles (NPs) into superstructures has emerged as an important strategy toward generating new functional materials.[1–6] The obtained hetero-superstructures integrate distinct components and often exhibit unanticipated properties with potential application in photonics,[7–12] magnetics,[13,14] catalysis,[15,16] and biomedicine.[17–21] However, the lack of a scalable assembly method limits broad application of hetero-superstructures. Current routes to hetero-superstructures are molecular linker-mediated NP conjugation and electrostatic attraction-induced NP assembly. For example, molecules with surface-seeking groups such as –SH and –NH$_2$ are usually used as linkers to assemble core–satellite super-structures.[22–25] DNA hybridization[17,19,26–30] and metal–phenolic coordination[31,32] are also well-established linker-mediated NP conjugation methods to assemble superstructures. In electro-static assembly, Coulomb forces between oppositely charged NPs are the driving forces of forming superstructures.[25,33–36]

Besides, entropy-driven assembly could generate NP super-lattices that consist of different types of NP building blocks,[37–39] but has not yet been exploited for core–satellite superstructures.

Despite the progressive assembly methods, the following 3 limitations have restricted the general assembly of hetero-superstructures using arbitrary building block materials: (1) highly specific assembly principles, such as thiol–metal bonding and complementary DNA strand hybridization, result in a limited assembly scope. A general approach with the driving force based on common properties of all NPs has been lacking. (2) Retained assembly additives in the obtained superstructures mask the original nature of the building blocks. The linkers which bring together the different building blocks could not be removed after assembly. Otherwise, the assembled material would be dissociated. (3) Complex assembly proce-dures seriously decrease the yield of assembly. The washing steps of NPs in the assembly, typically multiple centrifugations and resuspensions, result in aggregation of NPs in the sediment and loss of NPs in the discarded supernatant.

Here, we manipulate the interparticle balance between attraction and repulsion toward a simple and versatile method-ology for universal core–satellite superstructure assembly. The key step is using colloid destabilizers such as a nonpolar solvent or inorganic salt to reduce the stability (Coulomb repulsion) of one building block. Then the other building block acts as a new stabilizer to approach the destabilized building block *via* van der Waals (vdW) attraction (Fig. 1a). In contrast to previously reported methods, our assembly does not need any molecular linkers to

[a]Key Lab of Advanced Energy Materials Chemistry (Ministry of Education), Tianjin Key Lab of Molecular Recognition & Biosensing, Renewable Energy Conversion and Storage Center, College of Chemistry, Nankai University, Weijin Rd. 94, Tianjin 300071, China. E-mail: wei.xie@nankai.edu.cn

[b]School of Medicine, Nankai University, Weijin Rd. 94, Tianjin 300071, China

[c]National Center for Materials Service Safety, University of Science and Technology Beijing, Beijing 100083, China
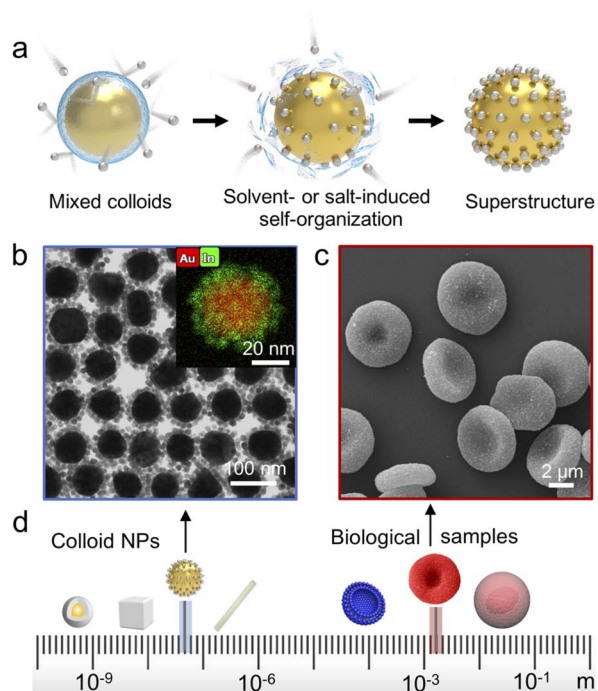
Fig. 1 Preparation of superstructures. (a) Schematic illustration of the core–satellite superstructure assembly. (b) TEM image and EDS mapping of Au@In$_2$O$_3$ core–satellite superstructures. (c) SEM image of the red blood cell (RBC)@Au core–satellite superstructures. (d) Schematic of building blocks with various shapes, sizes, compositions and functionalities.

bind the different building blocks together. Thus, the assembly process is extremely simple (only one step) and no additional substance is retained in the obtained core–satellite superstructures. Because vdW forces ubiquitously exist in all colloids, this methodology could in principle be used for assembly of any kinds of NPs in a colloidal suspension (Fig. 1b–d).

Results and discussion

Citrate-stabilized Au NPs[40] maintain colloidal stability *via* the strong interparticle repulsive forces (Fig. S1a and b†). When a nonpolar solvent such as hexane or toluene is added into the Au NPs dispersed in ethanol/isopropanol, a broad extinction band appears at ∼800 nm (Fig. S1d†) and the hydrodynamic diameter gradually increases due to partial coalescence of the Au NPs (Fig. S2†). The nonpolar solvent unambiguously breaks down colloidal stability by reducing repulsive forces and thus triggers NP self-organization. As a proof of concept, the citrate-stabilized Au NPs suspended in isopropanol/ethanol and oleylamine-stabilized In$_2$O$_3$ NPs suspended in hexane were selected as our model building blocks. By simply mixing the 2 colloids together, highly monodispersed binary Au$_{core}$–In$_2$O$_{3satellite}$ superstructures were obtained. We observed an obvious Au plasmon band shift after In$_2$O$_3$ approached (Fig. S3†) because of the dielectric environment change.

This assembly methodology is generally applicable and superstructures can be rationally designed using distinct building blocks. Fig. 2 shows diverse examples of superstructured nanomaterials. On quasi-spherical 80 nm Au NPs, different metal-based materials, including monometallic, alloy, oxide, sulfide, and perovskite NPs (Fig. 2a–d, j and S4–S11†), could easily be assembled as satellites. NPs having different morphologies such as Au–Ag core–shells, Au nanopeanuts, CdS nanowires, and Ag nanocubes could also be used as cores for superstructure assembly (Fig. 2f–i and S12–S15†).

Greatly encouraged by these experimental results, we extended this methodology to the assembly of organic and even biological nanoarchitectures. Polydopamine (PDA) NPs have been widely used in catalysis, medical imaging, cancer therapy, and antibacterial coating because of their antioxidant activity and strong metal-ion chelation.[41] We mixed PDA NPs with SiO$_2$ NPs suspended in ethanol and obtained organic–inorganic hybrid core–satellite superstructures by adding hexane (Fig. 2k and S16†). However, in the assembly of biological nano-architectures, nonpolar solvents cannot be used because they
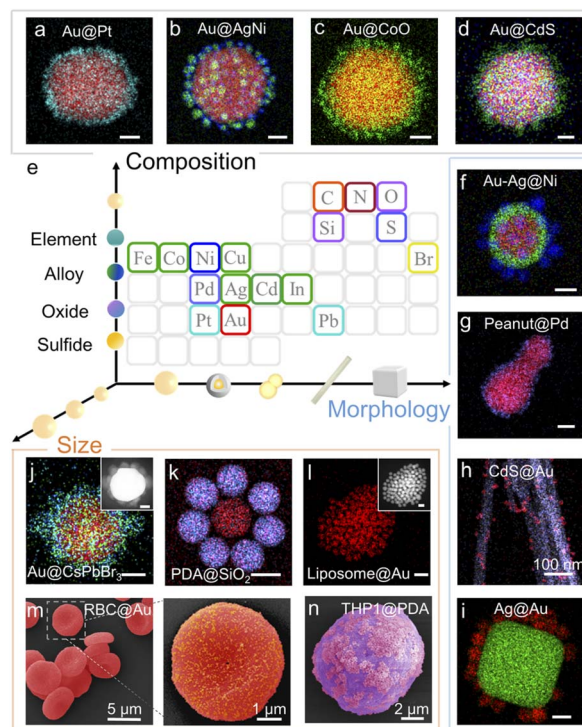

Fig. 2 Diversity of superstructured materials. (a–d) Elemental mapping images of Au@Pt (a), Au@AgNi (b), Au@CoO (c), and Au@CdS core–satellite superstructures (d). Scale bar, 20 nm. (e) Illustration of assembly using building blocks of diverse compositions, morphologies and sizes. (f–l) Elemental mapping images of Au–Ag@Ni (f), Au peanut@Pd (g), CdS@Au (h), Ag nanocube@Au(i), and Au@CsPbBr$_3$ perovskite (j) core–satellite superstructures. Scale bar, 20 nm. (k) Elemental mapping image of the PDA@SiO$_2$ core–satellite superstructure. Scale bar, 200 nm. (l) Elemental mapping image of the liposome@Au core–satellite superstructure. Scale bar, 20 nm. Insets of J and L are high-angle annular dark-field (HAADF) images of the corresponding superstructures. Scale bar, 20 nm. (m and n) Colored SEM images of RBC@Au (m) and living THP1 cell@PDA (n) biological core–satellite superstructures. The colors of the elements in the EDS mapping are marked on the periodic table in (e).

typically denature the biological building blocks. Thus, we used biocompatible phosphate buffer solution (PBS) to trigger self-organization. The ions in PBS neutralize the surface charge of colloidal NPs, instead of detaching the surface ligand, to weaken the repulsive forces and reduce their colloidal stability (Fig. S17†).[42,43] We obtained nanoarchitectures such as liposome$_{core}$@Au$_{satellite}$, red blood cell (RBC)$_{core}$@Au$_{satellite}$ and living THP1 cell$_{core}$@PDA$_{satellite}$ superstructures (Fig. 2l–n and S18–S20†). This process is very gentle and the living mammalian cells maintained their structural stability after assembly (Fig. S20†). Therefore, our methodology shows good applicability and can realize the assembly of superstructures with satellite numbers ≥6 and a core/satellite size ratio from 1 to ~200. The products are very robust and the core–satellite structure remains stable after vigorous ultrasonication, solvent-replacement and even 1 year aging at room temperature (Fig. S21†).

As a demonstration of preparing high-diversity super-structured materials, a co-assembly strategy was used to assemble superstructures with multiple types of satellites on the same core. We obtained a series of superstructures using the same batch of Au NP cores, including Au$_{core}$@Ag$_{satellite}$, Au$_{core}$@(Ag + Ni)$_{satellite}$, Au$_{core}$@(Ag + Ni + In$_2$O$_3$)$_{satellite}$, and Au$_{core}$@(Ag + Ni + In$_2$O$_3$ + Pt)$_{satellite}$ superstructures (Fig. 3a–d). Alternatively, multiple satellites can be assembled via a super-assembly strategy. For example, when RBC$_{core}$@PDA$_{satellite}$ superstructures were further used as the core in a second-round

assembly, Au NPs could be loaded as the second satellites (Fig. 3e–g). Any change in the type and sequence of satellites will result in new core–satellite superstructures.

To explore the mechanism behind this methodology, we further investigated the driving force of the solvent-induced superstructure assembly. In our control experiments, cores and satellites with the same charge could also form super-structures on the addition of hexane (Fig. S23†). In contrast, when hexane was absent, even the oppositely charged Au and In$_2$O$_3$ NPs could not form superstructures (Fig. S22 and S24†), which confirms that the assembly is not driven by electrostatic attraction. In the Fourier transform infrared (FTIR) spectra (Fig. 4a), the absorption band assigned to the asymmetric stretching of carboxylic groups of the citrate ligand redshifts from 1585 to 1558 cm^{-1},[44] indicating that the addition of hexane induces the attenuation of the intermolecular hydrogen bonds and disrupts the solvation of citrate molecules with iso-propanol (Fig. S25†). As shown in Fig. 4b the citrate ligand forms approximately four molecular layers on the Au NP surface after drying on a TEM grid;[45] in contrast, no obvious ligand shell is observed on hexane-treated NPs (Fig. 4c). Although the results were not measured from NPs in a colloidal suspension, it is clear that the hexane solvent removes most of the ligand molecules on the NP surface. Since non-polar solvents such as hexane are aimed at destroying citrate molecules, this
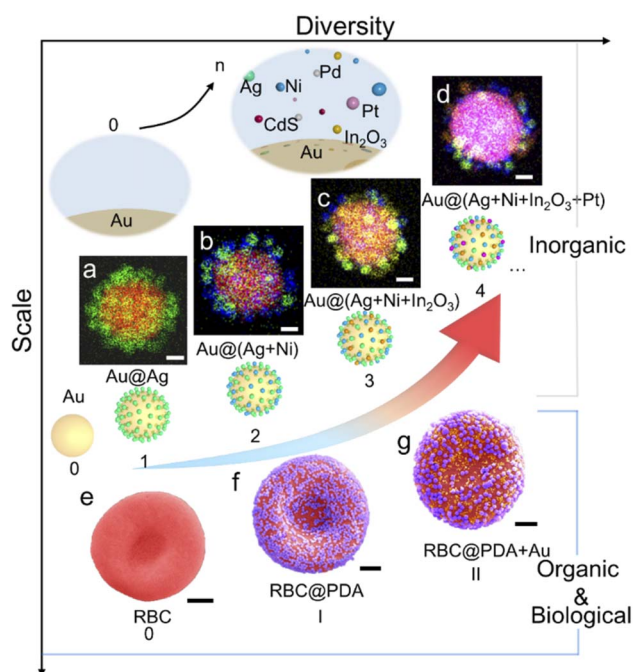

Fig. 3 High-diversity superstructure assembly. (a–d) Elemental mapping images of core–satellite superstructures with up to 4 types of satellites co-assembled on an 80 nm Au core: Au@Ag (a), Au@Ag + Ni (b), Au@Ag + Ni + In$_2$O$_3$ (c), and Au@Ag + Ni + In$_2$O$_3$ + Pt (d). Scale bar, 20 nm. (e–g) Colored SEM images of a red blood cell (e) and corresponding superstructures with PDA NPs (f) and PDA + Au NPs (g) as the satellites (scale bar, 1 μm).
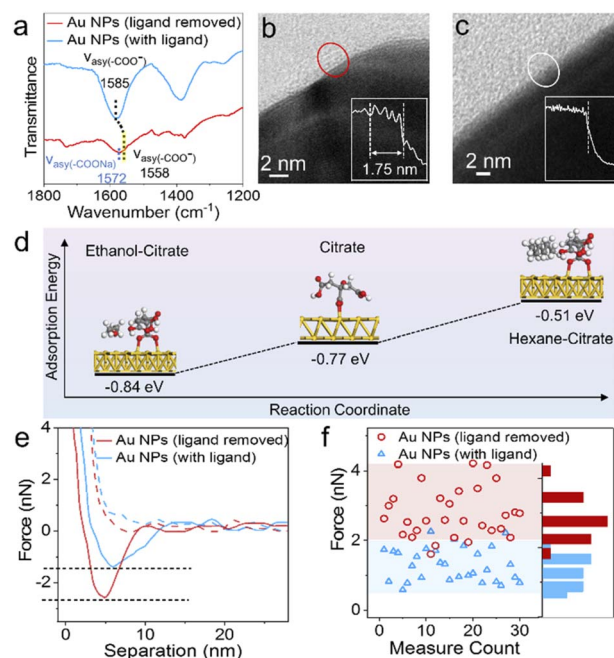

Fig. 4 Driving force of superstructure assembly. FTIR spectra (a), high-resolution transmission electron microscope (HRTEM) images and line scans of a citrate ligand adsorbed on the surface of Au NPs before (b) and after (c) treatment with hexane. (d) Adsorption energy of citrate on the Au NP surface in different solvent environments. (e) Force-distance curves measured using a Pt coated AFM tip on Au NPs before (cyan) and after (red) hexane treatment. The approach and retraction are presented with dashed and solid lines, respectively. (f) Scatter plot of adhesive force measurements on 60 Au NPs.

methodology is suitable for the assembly of citrate-capped NPs. We further used density functional theory (DFT) calculations (see the ESI for the detailed calculation process†) to evaluate the adsorption energy ($E_{ads} = -0.77$ eV) of a citrate ligand on the Au(111) surface (Fig. 4d). While ethanol solvent makes the surface ligand more stable ($E_{ads} = -0.84$ eV), the presence of hexane obviously weakens the adsorption of citrate ($E_{ads} = -0.51$ eV) on the Au(111) surface. The surface ligand has an important bearing on the colloidal stability of NPs.[46,47] ζ-Potential change of the Au NPs from -32.2 to -7.04 mV was observed within 12 min upon the addition of hexane (Fig. S2†).

The assembly process of the above core–satellite superstructures comprises two steps. First, one of the colloidal building blocks is destabilized. Second, the other building block acts as a new stabilizing agent and self-organizes around the first building block, which is likely driven by vdW forces. We used atomic force microscopy (AFM) to examine the vdW forces between the core and satellite.[48] A Pt tip (Fig. S27†) interacts with a Au core to simulate the Pt satellite of the Au$_{core}$@Pt$_{satellite}$ superstructure. An approach-retraction loop test was performed in a liquid environment. As shown in Fig. 4e, the Au NP surface treated with hexane exhibited twice the attractive force (2.6 nN) during tip retraction compared with its untreated counterpart (1.3 nN), corresponding to a higher energy of adhesion work ($E = 1.17 \times 10^{-2}$ vs. 6.85×10^{-3} fJ). The 60 tests on different Au NPs (Fig. 4f and S29†) suggested that the addition of hexane resulted in an appreciable attraction between the core and satellite NPs. Hexane acts as a ligand detacher and this role could also be played by other nonpolar solvents such as toluene, benzene and cyclohexane (Fig. S30†).

In classic Derjaguin–Landau–Verwey–Overbeek (DLVO) theory,[49] two major interactions (electrostatic repulsion and vdW attraction) determine the colloidal stability of a NP suspension. In our assembly, a third interaction of short-range repulsion resulting from steric hindrance of interfacial molecules is involved.[50,51] Eqn (1) describes the total interaction potential energy (V_{tot}) between Au and Pt NPs, which consists of electrostatic energy (V_{elec}), vdW potential energy (V_{vdW}) and short-range repulsion energy (V_{Born}):

$$V_{tot} = V_{elec} + V_{vdW} + V_{Born} \tag{1}$$

As shown in Fig. 5a, for Au and Pt NPs suspended in a hexane–ethanol mixture, the total potential energy minimum appears at ~0.23 nm (see the ESI for the detailed calculation process†). This value is consistent with the measured distance of ~0.30 nm between the Au core and Pt satellite (Fig. 5b). In contrast, the two building blocks maintain their colloidal state when hexane is absent due to the very shallow potential energy well.

Another important issue is the selective collision between the hetero-building blocks. In a binary colloid comprising two building blocks (A and B), there are 3 different collision directions, i.e. A–A, B–B and A–B collisions, among which only the third favors hetero-assembly. For example, in a mixed colloid of 80 nm Au and 10 nm Pt spheres, ~70 completely inelastic collisions between Au and Pt result in the formation of a core–
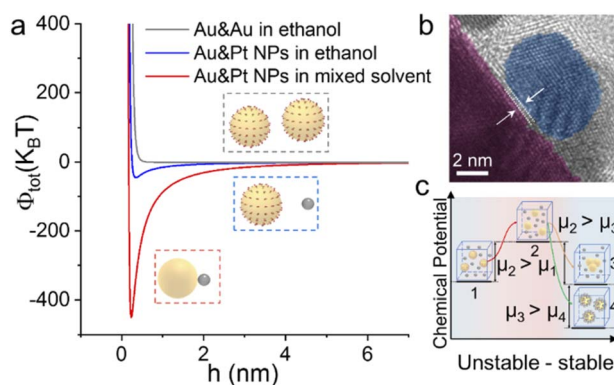

Fig. 5 (a) Total colloidal potential energy of Au + Pt NPs suspended in ethanol (blue) and an ethanol–hexane mixture (red) as a function of interparticle distance. The gray curve is the energy of the Au colloid before assembly. (b) HRTEM image of the Au$_{core}$@Pt$_{satellite}$ superstructure showing the distance between the Au core and Pt satellites. (c) Illustration of the chemical potential change of the colloidal mixture from the original steady state to the final steady state after assembly.

satellite superstructure (Fig. S4†) and the kinetic energy loss of the whole system is converted to heat. We can estimate the Gibbs free energy change according to the equation $\Delta G = \Delta H - T\Delta S$, in which ΔH and ΔS are enthalpy and entropy changes, respectively. The formation of a core–satellite superstructure (A–B) results in a lower Gibbs free energy than that in the formation of A–A or B–B clusters, indicating that the ligand-stripped Au core NPs intend to adsorb Pt NPs rather than self-aggregate (see the ESI for the detailed calculation process†). In view of thermodynamics, the unstable Au NPs after hexane treatment increased the chemical potential of the system from μ_1 to μ_2 (Fig. 5c). After this, the colloidal mixture reached a new steady state via self-organization of NPs. The selective collision of hetero-building blocks to form a superstructure is favored because of the lower chemical potential.

Finally, as a proof of concept, we showed the specific properties of superstructures based on assembly. Surface-enhanced Raman spectroscopy (SERS) is a sensitive analytical technique in the detection of trace chemical species. Normally, an SERS signal can only be detected from highly localized areas such as edges, tips of nanostructures and gaps between NPs. As shown in Fig. 6a, the Au@Au superstructure exhibits single-particle SERS sensitivity due to the plasmonic coupling between building blocks. In contrast, the corresponding 80 nm Au core does not enhance the Raman signal of reporter molecules under otherwise same conditions (Fig. S31†). Based on the sensitivity test, the detection limit of 4-nitrothiophenol and dye molecules (crystal violet) on the Au@Au superstructure can be acheived at 10^{-7} M (Fig. S32†). We further used Au@Pt superstructures with SERS activity to detect trace adsorbed H species in Pt-catalyzed hydrogen evolution reactions. The Pt–H band at around ~2060 cm^{-1} red-shifts with the decreasing potential (Fig. S33†), showing the exciting potential of studying electrocatalysis using core–satellite superstructures. In another example, we demonstrated enhanced photocatalytic activity enabled by assembly of semiconductor@metal (CdS@Au) superstructures. Due to the
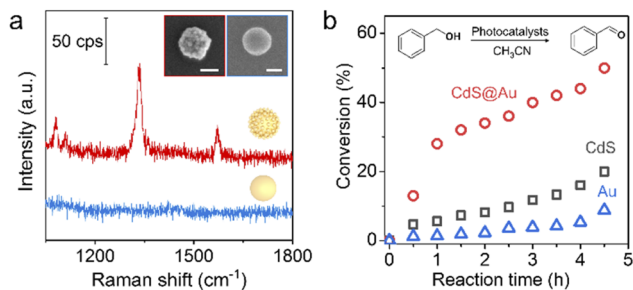
Fig. 6 (a) SERS spectra of 4-nitrothiophenol measured on a single Au@Au core–satellite superstructure (red) and the corresponding Au core (blue). (Inset) SEM images of a single superstructure (left) and a single Au core (right). Scale bar, 50 nm. (b) Conversion rate of benzyl alcohol in a photo-oxidation reaction catalyzed by Au NPs, CdS nanowires and CdS@Au superstructures, respectively.

efficient charge transfer at the metal–semiconductor interfaces, the superstructures exhibit enhanced photocatalytic performance with high stability in benzyl alcohol oxidation compared with the un-assembled building blocks (Fig. 6b and S34†).

Conclusions

To summarize, assembly of complex core–satellite superstructures is now a very simple task under our vdW force-driven assembly methodology. By weakening the repulsion between building blocks *via* detaching the ligand from their surfaces or neutralizing their surface charges, we trigger self-organization of small satellites on the surface of a large core. This assembly process does not involve additional molecular linkers that will be retained in the assembled superstructures. The agents used to destabilize the building blocks are nonpolar solvents or soluble inorganic salts and they can be completely removed after simple washing steps. Thus, the original nature of building blocks can be preserved after assembly. Using this facile and versatile approach, we obtained a library of distinct core–satellite superstructures. The assembly scope can be readily extended to a tremendous number of building blocks ranging from inorganic NPs to living cells, which offers great potential for application in fields such as catalysis, sensing, bioengineering, drug delivery, and others.

Data availability

All data are provided in the ESI† and additional data can be available upon request.

Author contributions

Wei Xie directed all aspects of the project. Wei Xie, Yanfang Hu, and Yonglong Li conceived the project. Yanfang Hu performed the superstructure assembly. Yanfang Hu, Yonglong Li, Linfeng Yu, and Yuying Zhang performed the characterization of the superstructures. Wei Zhang performed the characterization of ligands on the Au nanoparticle surface. Yanfang Hu and Yuming Lai performed the AFM measurement. Wei Xie and Yanfang Hu wrote the manuscript with input from all co-authors.

Conflicts of interest

The authors declare that they have no known competing financial interests or personal relationships that could have appeared to influence the work reported in this paper.

Notes and references

1 T. Udayabhaskararao, T. Altantzis, L. Houben, M. Coronado-Puchau, J. Langer, R. Popovitz-Biro, L. M. Liz-Marzán, L. Vuković, P. Král, S. Bals and R. Klajn, *Science*, 2017, **358**, 514–518.
2 A. M. Kalsin, M. Fialkowski, M. Paszewski, S. K. Smoukov, K. J. M. Bishop and B. A. Grzybowski, *Science*, 2006, **312**, 420–424.
3 N. Thi, M. Fayna and A. Souad, *Nanomaterials*, 2018, **8**, 149.
4 M. Grzelczak, L. M. Liz-Marzán and R. Klajn, *Chem. Soc. Rev.*, 2019, **48**, 1342–1361.
5 C. Yi, H. Liu, S. Zhang, Y. Yang, Y. Zhang, Z. Lu, E. Kumacheva and Z. Nie, *Science*, 2020, **369**, 1369–1374.
6 J. Jia, G. Liu, G. Xu, X. Tian, S. Li, F. Han, Y. Feng, X. Dong and H. Chen, *Angew. Chem., Int. Ed.*, 2020, **59**, 14443–14448.
7 R. P. M. Höller, M. Dulle, S. Thomä, M. Mayer, A. M. Steiner, S. Förster, A. Fery, C. Kuttner and M. Chanana, *ACS Nano*, 2016, **10**, 5740–5750.
8 F. Han, S. R. C. Vivekchand, A. H. Soeriyadi, Y. Zheng and J. J. Gooding, *Nanoscale*, 2018, **10**, 4284–4290.
9 Y. Zhao, L. Du, H. Li, W. Xie and J. Chen, *J. Phys. Chem. Lett.*, 2019, **10**, 1286–1291.
10 K. Zhang, L. Yang, Y. Hu, C. Fan, Y. Zhao, L. Bai, Y. Li, F. Shi, J. Liu and W. Xie, *Angew. Chem., Int. Ed.*, 2020, **59**, 18003–18009.
11 K. Sokołowski, J. Huang, T. Földes, J. A. McCune, D. D. Xu, B. de Nijs, R. Chikkaraddy, S. M. Collins, E. Rosta, J. J. Baumberg and O. A. Scherman, *Nat. Nanotechnol.*, 2021, **16**, 1121–1129.
12 Y. Chen, Y. Hu, J. Zhao, Y. Deng, Z. Wang, X. Cheng, D. Lei, Y. Deng and H. Duan, *Adv. Funct. Mater.*, 2020, **30**, 2000642.
13 E. A. Kwizera, E. Chaffin, X. Shen, J. Chen, Q. Zou, Z. Wu, Z. Gai, S. Bhana, R. O'Connor, L. Wang, H. Adhikari, S. R. Mishra, Y. Wang and X. Huang, *J. Phys. Chem. C*, 2016, **120**, 10530–10546.

14 S. N. Sheikholeslami, H. Alaeian, A. L. Koh and J. A. Dionne, *Nano Lett.*, 2013, **13**, 4137–4141.

15 J. Fu, W. Zhu, Y. Chen, Z. Yin, Y. Li, J. Liu, H. Zhang, J.-J. Zhu and S. Sun, *Angew. Chem., Int. Ed.*, 2019, **58**, 14100–14103.

16 Y. Li, Y. Hu, F. Shi, H. Li, W. Xie and J. Chen, *Angew. Chem., Int. Ed.*, 2019, **58**, 9049–9053.

17 C. Liu, C. Chen, S. Li, H. Dong, W. Dai, T. Xu, Y. Liu, F. Yang and X. Zhang, *Anal. Chem.*, 2018, **90**, 10591–10599.

18 H. S. Choi, *Nat. Nanotechnol.*, 2014, **9**, 93–94.

19 L. Y. T. Chou, K. Zagorovsky and W. C. W. Chan, *Nat. Nanotechnol.*, 2014, **9**, 148–155.

20 Z. Zhao, D. C. Pan, Q. M. Qi, J. Kim, N. Kapate, T. Sun, C. W. Shields IV, L. L.-W. Wang, D. Wu, C. J. Kwon, W. He, J. Guo and S. Mitragotri, *Adv. Mater.*, 2020, **32**, 2003492.

21 A. Huefner, W.-L. Kuan, K. H. Müller, J. N. Skepper, R. A. Barker and S. Mahajan, *ACS Nano*, 2016, **10**, 307–316.

22 S. Lee, M. Kim and S. Yoon, *Chem. Commun.*, 2019, **55**, 1466–1469.

23 W. Xie, B. Walkenfort and S. Schlücker, *J. Am. Chem. Soc.*, 2013, **135**, 1657–1660.

24 N. Gandra, A. Abbas, L. Tian and S. Singamaneni, *Nano Lett.*, 2012, **12**, 2645–2651.

25 S. Mühlig, A. Cunningham, S. Scheeler, C. Pacholski, T. Bürgi, C. Rockstuhl and F. Lederer, *ACS Nano*, 2011, **5**, 6586–6592.

26 N. Li, Y. Shang, Z. Han, T. Wang, Z. G. Wang and B. Ding, *ACS Appl. Mater. Interfaces*, 2019, **11**, 13835–13852.

27 S. J. Tan, M. J. Campolongo, D. Luo and W. Cheng, *Nat. Nanotechnol.*, 2011, **6**, 268–276.

28 L.-A. Wu, W.-E. Li, D.-Z. Lin and Y.-F. Chen, *Sci. Rep.*, 2017, **7**, 13066.

29 R. C. Mucic, J. J. Storhoff, C. A. Mirkin and R. L. Letsinger, *J. Am. Chem. Soc.*, 1998, **120**, 12674–12675.

30 X. Xu, N. L. Rosi, Y. Wang, F. Huo and C. A. Mirkin, *J. Am. Chem. Soc.*, 2006, **128**, 9286–9287.

31 J. Guo, B. L. Tardy, A. J. Christofferson, Y. Dai, J. J. Richardson, W. Zhu, M. Hu, Y. Ju, J. Cui, R. R. Dagastine, I. Yarovsky and F. Caruso, *Nat. Nanotechnol.*, 2016, **11**, 1105–1111.

32 J. Guo, M. Suástegui, K. K. Sakimoto, V. M. Moody, G. Xiao, D. G. Nocera and N. S. Joshi, *Science*, 2018, **362**, 813.

33 A. S. De Silva Indrasekara, S. J. Norton, N. K. Geitner, B. M. Crawford, M. R. Wiesner and T. Vo-Dinh, *Langmuir*, 2018, **34**, 14617–14623.

34 H. Zhang, C. Wang, H.-L. Sun, G. Fu, S. Chen, Y.-J. Zhang, B.-H. Chen, J. R. Anema, Z.-L. Yang, J.-F. Li and Z.-Q. Tian, *Nat. Commun.*, 2017, **8**, 15447.

35 H. Zhang, X. G. Zhang, J. Wei, C. Wang, S. Chen, H. L. Sun, Y. H. Wang, B. H. Chen, Z. L. Yang, D. Y. Wu, J. F. Li and Z. Q. Tian, *J. Am. Chem. Soc.*, 2017, **139**, 10339–10346.

36 D. A. Walker, E. K. Leitsch, R. J. Nap, I. Szleifer and B. A. Grzybowski, *Nat. Nanotechnol.*, 2013, **8**, 676–681.

37 C. J. Kiely, J. Fink, M. Brust, D. Bethell and D. J. Schiffrin, *Nature*, 1998, **396**, 444–446.

38 E. V. Shevchenko, D. V. Talapin, N. A. Kotov, S. O'Brien and C. B. Murray, *Nature*, 2006, **439**, 55–59.

39 D. V. Talapin, E. V. Shevchenko, M. I. Bodnarchuk, X. Ye, J. Chen and C. B. Murray, *Nature*, 2009, **461**, 964–967.

40 N. G. Bastús, J. Comenge and V. Puntes, *Langmuir*, 2011, **27**, 11098–11105.

41 Z. Wang, Y. Zou, Y. Li and Y. Cheng, *Small*, 2020, **16**, 1907042.

42 G. I. Guerrero-García, P. González-Mozuelos and M. Olvera de la Cruz, *ACS Nano*, 2013, **7**, 9714–9723.

43 Z. Zhang, S. Maji, A. B. d. F. Antunes, R. De Rycke, Q. Zhang, R. Hoogenboom and B. G. De Geest, *Chem. Mater.*, 2013, **25**, 4297–4303.

44 Z. Lee, K.-J. Jeon, A. Dato, R. Erni, T. J. Richardson, M. Frenklach and V. Radmilovic, *Nano Lett.*, 2009, **9**, 3365–3369.

45 J.-W. Park and J. S. Shumaker-Parry, *J. Am. Chem. Soc.*, 2014, **136**, 1907–1921.

46 H. Kang, J. T. Buchman, R. S. Rodriguez, H. L. Ring, J. He, K. C. Bantz and C. L. Haynes, *Chem. Rev.*, 2019, **119**, 664–699.

47 H. Al-Johani, E. Abou-Hamad, A. Jedidi, C. M. Widdifield, J. Viger-Gravel, S. S. Sangaru, D. Gajan, D. H. Anjum, S. Ould-Chikh, M. N. Hedhili, A. Gurinov, M. J. Kelly, M. El Eter, L. Cavallo, L. Emsley and J.-M. Basset, *Nat. Chem.*, 2017, **9**, 890–895.

48 B. Li, J. Yin, X. Liu, H. Wu, J. Li, X. Li and W. Guo, *Nat. Nanotechnol.*, 2019, **14**, 567–572.

49 T. Hueckel, G. M. Hocky, J. Palacci and S. Sacanna, *Nature*, 2020, **580**, 487–490.

50 Y. Liu, X. Han, L. He and Y. Yin, *Angew. Chem., Int. Ed.*, 2012, **51**, 6373–6377.

51 J.-A. Park and S.-B. Kim, *J. Contam. Hydrol.*, 2015, **181**, 131–140.